Tuning the Interfacial Mechanical Behaviors of Monolayer Graphene/PMMA Nanocomposites

Guorui Wang,[†,‡] Zhaohe Dai,[‡,§] Luqi Liu,[*,‡] Hai Hu,[‡] Qing Dai,[‡] and Zhong Zhang[*,‡]

[†]CAS Key Laboratory of Mechanical Behavior and Design of Materials, Department of Modern Mechanics, University of Science and Technology of China, Hefei 230027, China

[‡]CAS Key Laboratory of Nanosystem and Hierarchical Fabrication, CAS Center for Excellence in Nanoscience, National Center for Nanoscience and Technology, Beijing 100190, China

[§]University of Chinese Academy of Science, Beijing 100049, China

Ⓢ *Supporting Information*

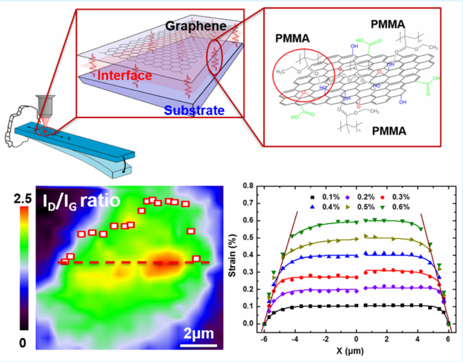

ABSTRACT: The van der Waals (vdW) force dominated interface between graphene and polymer matrix creates weak points in the mechanical sense. Chemical functionalization was expected to be an effective approach in transfer of the outstanding performance of graphene across multiple length scales up to the macroscopic level, due to possible improvements in the interfacial adhesion. However, published works showed the contradiction that improvements, insensitivity, or even worsening of macro-mechanical performance have all been reported in graphene-based polymer nanocomposites. Particularly central cause of such discrepancy is the variations in graphene/polymer interfacial chemistry, which is critical in nanocomposites with vast interfacial area. Herein, O_3/H_2O gaseous mixture was utilized to oxidize monolayer graphene sheet with controlled functionalization degrees. Hydrogen bonds (H bonds) are expected to form between oxidized graphene sheet/poly(methyl methacrylate) (PMMA) at the interface. On the basis of in situ tensile-micro Raman spectroscopy, the impacts of bonding types (vdW and H-bonds) on both key interfacial parameters (such as interfacial shear strength and critical length) and failure modes of graphene/PMMA nanocomposite were clarified for the first time at the microscopic level. Our results show that owing to improved interfacial interaction via H bonds, the interface tends to be stiffening and strengthening. Moreover, the mechanical properties of the functionalized graphene/PMMA interface will be set by the competition between the enhanced interfacial adhesion and the degraded elastic modulus of graphene, which was caused by structural defects in the graphene sheet during the functionalization process and could lead to catastrophic failure of graphene sheets in our experimental observation. Our results will be helpful to design various nanofiller-based nanocomposites with high mechanical performance.

KEYWORDS: *graphene, functionalization, Raman spectroscopy, interface, failure modes*

1. INTRODUCTION

Nanostructured carbon materials such as one-dimensional carbon nanotubes (CNT) and two-dimensional graphene sheets possess extremely high stiffness and strength, large surface area, high aspect ratio, low mass density, and have been envisaged to be the ideal reinforcement for polymer nanocomposites.[1−4] Over the past decades, considerable attention has been generated to fully utilize such extraordinary mechanical properties of nanofillers at a macroscopic level. To date, published works have shown that macro-mechanical performance of graphene-based polymer nanocomposites is far below theoretical expectation. Several key issues in nanofiller-based composites have to be addressed, such as the reinforcing role, the fracture modes, and interfacial properties. Classic view of conventional fiber-reinforced composites implies that the mechanical reinforcement of composites is not only determined by the intrinsic mechanical properties of reinforcing fillers but also strongly dependent on the interfacial adhesion quality between the filler and surrounding matrix.[5,6] Though graphene and CNT behaved remarkably in the former, it has been gradually recognized that the native interface between matrix and atomically smooth surface, dominated by vdW interaction, creates weak points in the mechanical transfer. Interfacial chemistry has been considered an effective approach to improve the interfacial adhesion between filler and polymer matrix, especially for nanostructured carbon material based systems where vast interfacial areas were created. Several strategies have been proposed to modify the nanostructured carbon material surfaces to strengthen the interfacial adhesion.[7−11] The apparently enhanced strength, stiffness, and fracture toughness have been observed for the functionalized carbon nanofiller-incorporated nanocomposite through

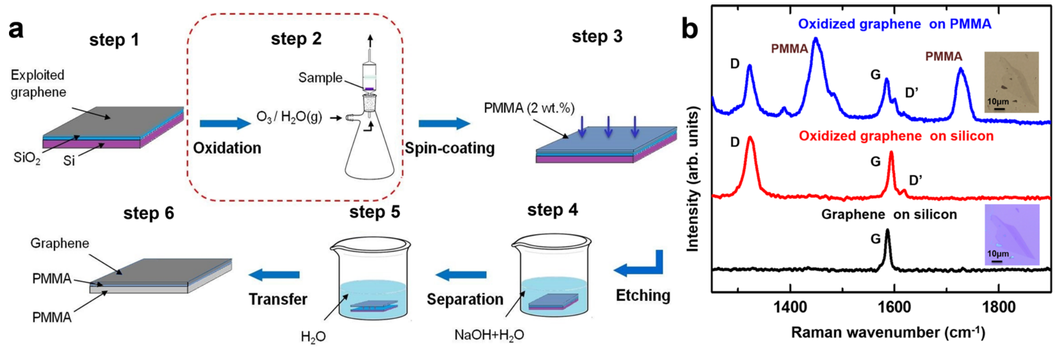

Figure 1. (a) Schematic illustration of the sample preparation process. For pristine graphene/PMMA nanocomposite systems, step 2 was skipped. (b) Raman spectra of pristine graphene sheet deposited onto silicon and oxidized graphene deposited onto silicon and PMMA substrates. The insets show optical images of the graphene sheet on silicon and PMMA substrates.

strong chemical bonds at the interface, while insensitivity or even worsening of macro-mechanical performance have all been reported.[12−14] Particularly central causes of such a contradiction are the variations in nanocarbon-polymer interfacial chemistry. This issue, also of importance in conventional fiber-reinforced composites, might be much more critical in nanocomposites due to their vast interfacial area. Thus, efforts to examine interfacial properties and then clarify the impact of interfacial bonding types (e.g., VdW forces, H bonds, covalent bonds, and coordinate bonds) on the interfacial mechanical behaviors are critical and indispensable for these nanoscale interfaces.

In conventional composite systems, the fiber-matrix stress transfer mechanism is relatively well understood by classic composite elastic models, and the interfacial properties are also well evaluated by various experimental methods.[5] By contrast, as the filler size dropped into nanoscale, monitoring the matrix-nanofiller (especially for two-dimensional graphene sheet) stress transfer is only in an initial stage. The nanopullout technique proposed by Wagner's group first measured the interfacial shear strength between individual nanotubes and polymer matrix with the value of 50 MPa, on the same level of conventional carbon fiber based composites.[15] However, experimentally, it is still challenging to directly measure the interfacial strength and then efficiency of stress transfer in the individual graphene sheet based interface because of its atomically thin shape and dimensions which invalidate the nanopullout techniques. Consequently, the underlying reinforcing mechanism as well as impact of interfacial bonding types on the interfacial properties and failure modes of graphene/polymer interface has not been deeply understood yet at the nanoscale.

Raman spectroscopy is a powerful tool to evaluate whether stress transfer takes place in conventional fiber (Carbon or Kevlar fiber)-based model composites as well as carbon nanostructured materials based nanocomposite systems through monitoring the specific peak shifts under strain.[5,16−18]

Our group has successfully employed in situ Raman measurements to assess the shear stress transfer and reveal the possible failure modes of macroscopic SWNT films and fibers as well as graphene papers.[19−22] Recently, through in situ Raman spectroscopy, the monolayer nature of graphene with micrometer lateral size makes it of particular promise for not only nanofiller but also sensor applications, allowing the direct measurement of the in-plane strain and hence the detection of interfacial behavior as well as speculating shear properties at the microscopic level.[23−31] For instance, we have investigated the in-plane biaxial compression behavior of PMMA/graphene/PMMA systems, and the compressive instability induced interfacial debonding was directly observed by in situ Raman spectroscopy.[30] Gong et al. have monitored the stress transfer in monolayer graphene sandwiched between the PMMA and the SU-8 polymer layer. The derived interfacial shear strength was on the order of 0.3−0.8 MPa, which is 2 orders of magnitude lower than that of the conventional carbon fiber material-based composites.[25] Similar results were also observed for monolayer graphene-based polyethylene terephthalate (PET) matrix nanocomposites.[29]

Herein, in situ tensile Raman spectroscopy is utilized and the impact of interfacial bonding types on the interfacial properties and failure modes of graphene/PMMA interface are systematically investigated for the first time at the microscopic level. In efforts to tune the interfacial adhesion through H-bond interactions, various oxygen-containing groups (e.g., hydroxyl groups, carboxylic groups, and epoxide groups) were introduced to the monolayer graphene surface and the functionalization degrees were exactly controlled. Our results show that the interfacial strength was measured to be improved with increasing functionalization degrees of the graphene sheet. However, plateau was also observed with further increasing functionalization degrees, and instead, the domain with oxygen-containing groups might act as defects to induce initiation and propagation of cracks of the graphene sheets during deformation. To the best of our knowledge, experimentally, it is first time to demonstrate that the impact of surface functionalization and functionalization degrees of nanofillers on the interfacial adhesion of nanocomposites clarifies the importance of optimized chemical functionalization on the interfacial stress transfer and fracture mechanism at a microscopic level. The results will provide valuable insight and design guidelines for high mechanical performance graphene and other nanofiller-based nanocomposites.

2. EXPERIMENTAL SECTION

2.1. Sample Preparation. The graphene samples were prepared by micromechanical cleavage[32] and adhered to Si wafer substrate with a 300 nm SiO$_2$ capping layer. Optical microscopy was used to locate the graphene sheet, and the corresponding thickness was further confirmed by Raman spectroscopy and atomic force microscopy (AFM). AFM images were recorded using a Dimension 3100 Veeco in the Peak Force tapping mode. Using the same method as reported in our earlier work,[30] a thin layer of PMMA (2 wt % in chloroform) was spin-coated on the substrate prior to the transfer. Afterward, the detachment of the PMMA−graphene layer from the initial surface was

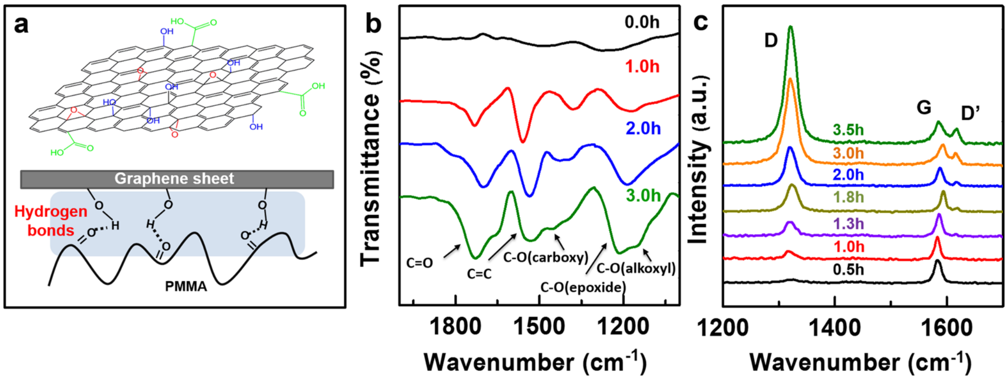

Figure 2. (a) Schematic of an oxidized graphene sheet having various oxygen-containing groups and interacting with the carbonyl groups of PMMA through hydrogen bonds. (b) FTIR spectra of oxidized graphene treated at different reaction times. (c) Raman spectra of oxidized graphene sheets treated at different reaction times.

done by partially etching the surface of SiO_2 with a 1 M NaOH aqueous solution. As a result, a PMMA membrane was obtained with all of the graphite/graphene sheets attached to it. Finally, the monolayer graphene sheet was then successfully transferred onto the surface of the PMMA bar as shown in Figure 1a. The close specific Raman peak positions as well as the constant Raman intensity ratio of I_D/I_G of oxidized graphene sheet as shown in Figure 1b indicates the success of the transfer process. Remarkably, the slight variations in Raman frequency (up to 3 cm^{-1}) might be due to the doping effect (Figure 1b). Meanwhile, the identical lateral size and shape of graphene sheets are observed in two substrates as shown in the inset of Figure 1b. Note, instead of embedding graphene sheet inside PMMA matrix, herein, the monolayer graphene sheet was exposed on top of PMMA beam, which would facilitate the morphology characterization by AFM before the tension and after the release.

2.2. Functionalization of Monolayer Graphene Sheet. Oxidization of individual graphene sheet was performed by using a O_3/H_2O gaseous mixture as an oxidizing agent based on our previous work.[33] An exfoliated graphene sheet deposited onto silicon wafer was placed into a homemade reactor, in which O_3 (5 wt % in O_3/O_2 mixture) was continuously passed through the reactor chamber at room temperature during the oxidation process. The oxygen gas flow rate was kept at 150 L/h, and the humidity inside the reactor was kept around 60% as monitored by a hygrometer. The reaction time was varied from 0.5 to 7 h to control the functionalization degree of graphene sheets. Microscopic fourier transform infrared spectrometer (FTIR) (Reflection mode) (ThermoFisher, Nicolet iN10) was employed to identify the various oxygen-containing groups attached on the graphene sheet. The Raman spectra were obtained with a Renishaw Raman spectrometer using the 514.5 nm line of an Ar laser. The laser power was kept below 1.0 mW on the sample to avoid laser-induced local heating of the sample. The incident light was polarized along the strain direction. The focused laser spot was approximately 1 μm in diameter, and the spectral resolution was ~1 cm^{-1}.

2.3. In Situ Tensile-Micro Raman Test. The mechanical deformation was carried out with a PMMA cantilever beam mounted onto a piezoelectric stage with a resolution of 600 nm in a Renishaw Raman spectroscope setup, as depicted in Figure S1. The tensile strain applied to the individual graphene sheet deposited on the top surface of the beam is given by the following eq 1,[34]

$$\varepsilon\left(x, \frac{t}{2}\right) = \frac{3t\delta(L - x)}{2L^3} \tag{1}$$

where x is the distance between the graphene sheet and the fixed end, t is the thickness of the beam, L is the span of the beam, and δ is the deflection of the beam at the load point. To ensure the validity of eq 1 experimentally, the aspect ratio of span to maximum deflection was ensured to be greater than 10 and the deformation strains were within the range from −1.5% to +1.5%.[35] It is noting that, due to the considerably small size, the strain gradient across the graphene flake along the cantilever beam was no more than 0.005% which could be neglected. Thus, the applied strain to the graphene flakes was supposed to be constant. In our experiment, the tensile strain was applied with an increment step of ~0.05% or ~0.1%. All bands in the Raman spectra of graphene were fitted with Lorentzian functions. To obtain the strain distribution based on the line profile of Raman 2D-band frequency, the tested monolayer graphene sheets were moved with a step size of 600 nm and Raman spectra from every spot of the sample were recorded. To convert the Raman 2D peak shift to strain, the rate of −51 cm^{-1}/% was used as a reference.

3. RESULTS AND DISCUSSION

3.1. Chemical Functionalization of Monolayer Graphene Sheet. In accordance with our previous work, the gaseous mixture of ozone and water vapor (O_3/H_2O) is jointly involved as an oxidizing reagent to oxidize the monolayer graphene sheet at room temperature.[33] The chemical oxidation is performed in a homemade reactor as illustrated in Figure 1a (step 2). Through a facial 1,3-dipolar cycloaddition reaction following the Griegge's mechanism, the oxygen-containing functional groups such as hydroxyl, carboxyl, and epoxy groups as shown in Figure 2a are successfully attached onto the surface of the graphene sheet.[36] Figure 2b shows the typical FTIR spectra of the graphene sheets treated by a O_3/H_2O gaseous mixture at different times. As expected, no apparent FTIR bands could be observed for a pristine graphene sheet due to its infrared inactive carbon−carbon double bonds. After oxidation treatment, the peak at 1720 cm^{-1} related to carbonyl groups, a broad band around 1200 cm^{-1} assigned to the coupling of ν(C−O) of alkoxyl and epoxide groups, and the stretching mode of ν(C═C) at 1580 cm^{-1} in the graphene backbone are observed.[22] With a further increasing oxidization time up to 3 h, the band intensity of carbonyl groups at 1720 cm^{-1} relative to that of the C═C backbone at 1580 cm^{-1} tended to increase, indicating an enhancement of oxygen-containing groups in the oxidized graphene samples. Meanwhile, the apparent Raman D-band and D′-band are observed for the oxidized graphene samples, implying the conversion of sp^2 carbon to sp^3 carbon due to the oxygen-containing functional groups grafted onto the graphene sheet.[37] Figure 2c shows the evolution of Raman D-band and D′-band intensity in the consecutive spectra, in which the continuous attachment of oxygenated groups onto graphene sheet leads to changes in the relative intensity of the D-band normalized to the G-band greatly. Earlier works have successfully utilized the intensity ratio between the Raman D-band and the G-band to quantify the covalent chemical

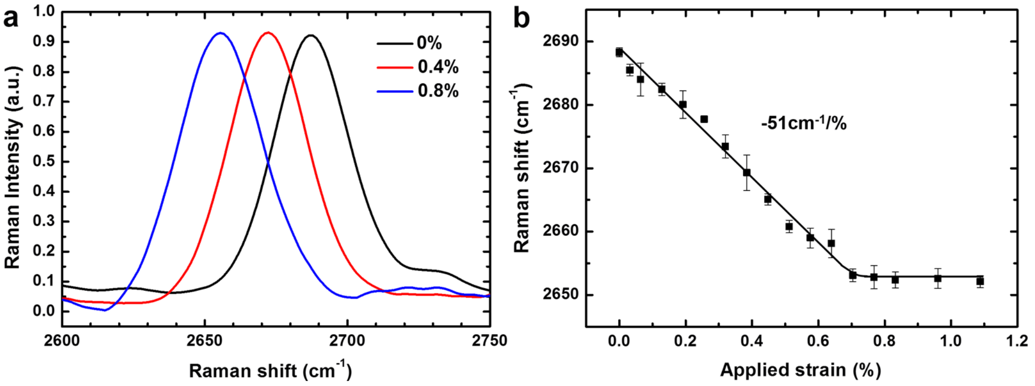

Figure 3. (a) Evolution of Raman 2D spectrum of monolayer graphene with increasing applied strain. (b) Raman 2D band tends to red shift linearly during tension at a rate of -51 cm^{-1}/% until reaching the strain of 0.7% and then step into a plateau which implies the occurrence of interfacial sliding.

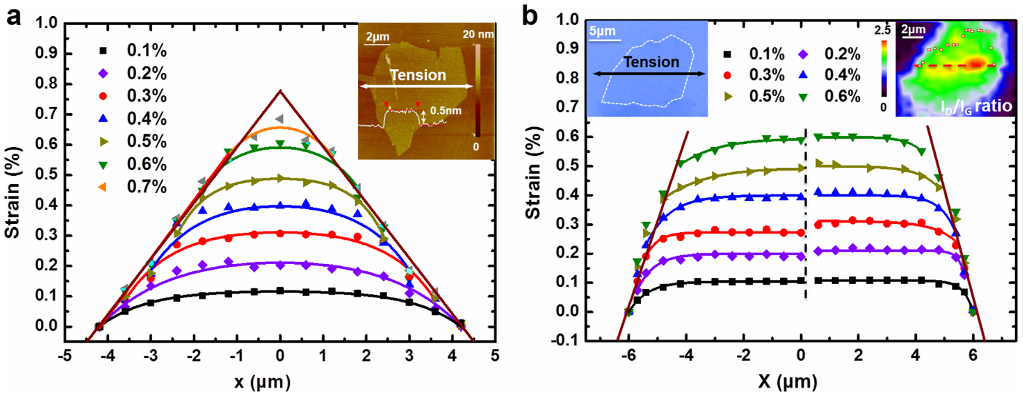

Figure 4. Strain distribution in the direction of the tensile axis of the (a) pristine graphene sheet and (b) oxidized graphene sheet at different strain levels. The insets are (a) the AFM image and (b, left panel) optical image of tested graphene sheets and (b, right panel) its corresponding Raman contour map of I_D/I_G. The Raman data points are fitted by the solid lines based on the nonlinear shear-lag model.

reorganization of the π bonds of graphene,[37] functionalization degree of arylated graphene,[38] and the amount of defects induced by ion bombardment.[39] As presented in Figure S2, a monotonically increased trend of the Raman intensity ratio of I_D/I_G as a function of reaction times was observed at earlier range, implying the increase in the functionalization degrees of the oxidized monolayer graphene sheets. Beyond certain reaction times, the Raman D′-band tended to merge into the G-band[39] and the Raman intensity ratio of I_D/I_G eventually reached a plateau region. Following the chemical oxidation treatment, the oxidized graphene sheet was then transferred from a rigid silicon substrate to a flexible PMMA substrate.

3.2. Investigation of Interfacial Adhesion between Oxidized Graphene/PMMA Nanocomposites. In situ tensile Raman measurement has been viewed as a versatile methodology to investigate the interfacial behavior of carbon nanomaterial-based nanocomposites at a microscopic level.[23,25,29] Here, a Raman 2D-band was selected to measure the local strain in graphene, considering its higher strain-induced shift compared with that of the Raman G-band. Figure 3a presents the evolution of the Raman 2D spectrum of monolayer graphene measured at the center of a graphene sheet, in which the frequencies are tempting to decline with increasing applied tensile strains. Figure 3b shows that the Raman 2D-band red shifts linearly at a rate of -51 cm^{-1}/% until reaching the strain level of 0.7% and then steps into a plateau which is ascribed to the interfacial sliding. Similar Raman peak shift rate was observed in a graphene/PET laminate.[29]

To describe the interfacial stress transfer process as well as its possible deformation modes in the monolayer graphene/polymer nanocomposite, the conventional shear lag model was utilized in earlier works as reported by Gong et al.[25] At low strain level, the graphene/PMMA interface was assumed to be elastic, and the strain distribution in the graphene sheet (ε_g) as a function of the position (x) along the length direction could be predicted by the following eq 2:

$$\varepsilon_g = \varepsilon_m\left[1 - \frac{\cosh(\beta L x/L)}{\cosh(\beta L/2)}\right] \tag{2}$$

where ε_m is the applied strain of bulk matrix, L is the length of graphene in the x direction with $x = 0$ at the center and $\beta = \sqrt{k_m/E_{2D}}$ is the shear-lag parameter depending on the effective interfacial stiffness k_m (also called effective stiffness of the near-graphene surface of the matrix)[29] and the in-plane stiffness of monolayer graphene E_{2D}. By Equation 2, it is suggested that the maximum strain of graphene occurred at the center ($x = 0$) and maximum interfacial shear stress occurred at the edges ($x = \pm L/2$). In accordance with our experimental results, at the relatively low strain level (e.g., $\varepsilon_m \leq 0.2\%$), the strain distribution of the graphene sheet can be fitted well by eq 2 with fitting parameter $\beta = 0.6$ as shown in Figure 4a. Beyond the critical sliding strain (ε_c), eq 2 no longer predicts the strain

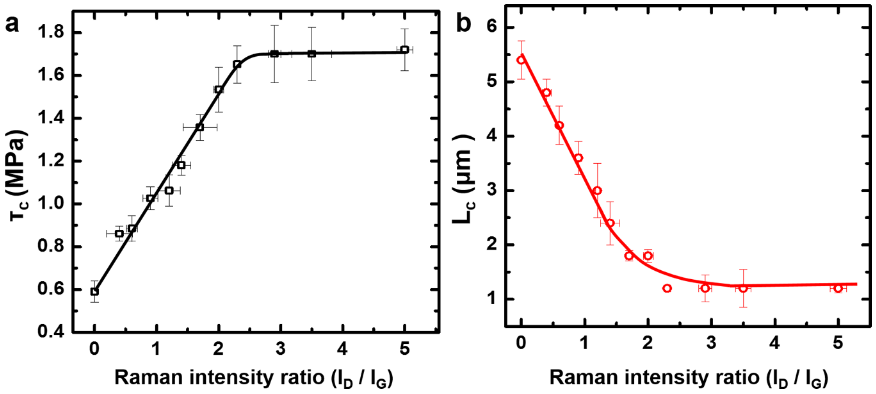

Figure 5. (a) The interfacial shear strength (τ_c) and (b) critical length as a function of the Raman intensity ratio of I_D/I_G in graphene/PMMA nanocomposite system. The solid lines are guided for eyes.

distribution in graphene sheet because the interfacial sliding occurs at the edges ($x = \pm L/2$). The maximum interfacial shear stress reached at the onset of interfacial sliding can be quantified by the interfacial shear strength (τ_c).

To describe the interface region which consists of two sliding zones emerged from the graphene sheet edges and an elastic (nonsliding) zone, a nonlinear shear lag model is proposed by considering interfacial sliding stress as a constant.[29,40] Recent works suggested that the repetitive reforming and breaking of interaction at the interface region would occur during the sliding process for both vdW and H-bond interaction.[41−43] In other words, the shear stress would be nearly equal to the shear strength and be kept constant. Therefore, the strain distribution near the edges of the graphene sheet would tend to be linear after the onset of interfacial sliding, and eventually, the strain distribution of the whole graphene sheet would tend to be triangle-like when the sliding zones develop to approach the center of the graphene sheet. Such interfacial sliding from the edges of the graphene sheet was observed in our in situ Raman mapping as evidenced by the almost linear strain distributions at sliding zones when increasing the applied strain levels after 0.2% as shown in Figure 4a. With further increasing the applied strain above 0.7%, the sliding zones progressively extend to the center of the graphene sheet and with the plateau strain (ε_p) of 0.7%. The interfacial shear strength (τ_c) can be derived based on the linear slope of the triangle-like strain distribution as presented by eq 3,

$$\tau_c = E_{\mathrm{gra}} t \frac{\mathrm{d}\varepsilon}{\mathrm{d}x} \approx E_{\mathrm{gra}} t \frac{\varepsilon_p}{L/2} \qquad (3)$$

where E_{gra} is 1 TPa, t is 0.35 nm[3,44] $\frac{\mathrm{d}\varepsilon}{dx}$is the slope of strain gradient in sliding zones. The interfacial shear strength in our graphene/PMMA nanocomposite system was on the level of 0.6 MPa, which was consistent with the values reported previously for a PMMA/graphene/SU8 laminate (0.3−0.8 MPa) and a graphene/PET laminate (0.7 MPa).[25,29] The relatively low interfacial shear strength indicates the poor stress transfer efficiency caused by vdW interaction between the graphene sheet and the surrounding matrix.

To enhance the interfacial shear strength in the graphene/PMMA nanocomposite, we utilize a O_3/H_2O gaseous mixture to oxidize graphene and build interfacial H bonds between the oxidized graphene sheet and the PMMA substrate. Earlier works have demonstrated that the pendant hydroxyl groups across the surface of graphene could form H bonds with the carbonyl groups of PMMA.[7,45] To reveal the effect of H bonds at the interface on the interfacial shear strength as well as its dependence on the functionalization degrees of the oxidized graphene sheet, herein, the monolayer graphene sheets with varied functionalization degrees are investigated. Figure 4b shows the strain distribution of oxidized monolayer graphene sheet along the dashed line at different applied strain levels. It can be seen from the fitting results that both the fitted β values and the corresponding slopes $\frac{\mathrm{d}\varepsilon}{\mathrm{d}x}$ for the oxidized graphene sheet are higher than those of the pristine graphene sheet having similar lateral sizes (e.g., $\beta = 2.5$ and $\frac{\mathrm{d}\varepsilon}{\mathrm{d}x} = 0.35\%/\mu\mathrm{m}$ vs $\beta = 0.6$ and $\frac{\mathrm{d}\varepsilon}{\mathrm{d}x} = 0.16\%/\mu\mathrm{m}$) This is a clear indication of the better stress transfer performance obtained for oxidized monolayer graphene sheet, which could be attributed to the formation of H bonds at the interface. The insets in Figure 4b present the optical image of the individual oxidized monolayer graphene sheet and its corresponding contour map of Raman intensity ratio (I_D/I_G). Obviously, within an individual oxidized monolayer graphene sheet, the red region shown in the right inset exhibits a higher functionalization degree than the yellow region. Thus, the local strain value in the red region appears a bit higher than that of yellow region, implying a relatively larger β value for the highly functionalized part ($\beta = 3.3$ vs $\beta = 2.5$ for H-bond interfaces and $\beta = 0.6$ for native interface).

In order to systematically clarify the influence of functionalization degrees of the oxidized monolayer graphene sheet on the interfacial properties of nanocomposites, in situ Raman measurements were performed for at least 9 samples with various lateral sizes and functionalization degrees. Detailed information is summarized in Table S1. Considering the nonuniform distribution of the functionalized groups in the individual oxidized monolayer graphene sheet, the standard deviation of the averaged Raman intensity ratio of I_D/I_G was analyzed based on at least 5 point tests at a given reaction time. Figure 5a shows the trend of the interfacial shear strength as a function of the Raman intensity ratio (I_D/I_G) of the oxidized graphene sheet. The τ_c tends to increase from 0.6 to 1.7 MPa linearly with the increasing Raman intensity ratio of I_D/I_G up to ∼3.0 and improves by nearly four times compared with previous results (averaged 0.4 MPa),[25,26,46] indicating that the H bonds at the interface enhances the interfacial adhesion unambiguously. With a further increasing Raman intensity ratio of I_D/I_G beyond ∼3.0, while the τ_c reaches a plateau region, indicating that the interfacial adhesion is hard to improve any

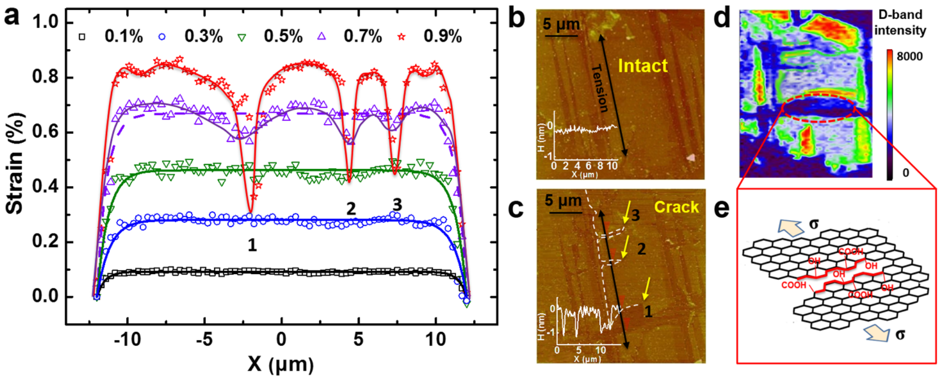

Figure 6. (a) Strain distribution of monolayer graphene with $I_D/I_G = 5$ at different strain levels. Cracks tend to occur at high strain levels. AFM images of oxidized graphene sheet (b) before the tension and (c) after the release; the insets show the height profile of the tested graphene sheet. (d) Raman image of D-band intensity of oxidized graphene sheet after tension. (e) Schematic illustrating the crack growth behavior of graphene provoked from tensile stress.

more. Similar phenomenon is also observed for the critical length (L_c), which shows a notable decline as presented in Figure 5b, followed by a plateau stage. Actually, L_c is the minimum length required to establish an isostrain condition between the graphene and the matrix via shear stress, and it is commonly taken as the double of the distance from the end to where the local strain reaches 95% of the maximum, as shown in Figure S3. Clearly, the reduced L_c is corresponding to higher β and hence the enhanced stress transfer efficiency, which results from the H-bond interactions. Note that the obtained L_c for the pristine graphene in our work is around 5.4 μm, which is approximated to the reported value (3 μm).[25] With an increasing Raman intensity ratio of I_D/I_G, L_c could decrease to as low as 1.2 μm. As mentioned earlier, the interfacial interaction between the pristine graphene sheet and the underlying polymer substrate is only vdW and is not strong enough to ensure efficient stress transfer. On the basis of our work, in efforts to take advantage of the very high Young's modulus and strength of the graphene sheet more effectively, it is essential to attach oxygenated groups onto the graphene sheet to strengthen the interfacial interaction between the graphene and the PMMA substrate via H bonds. However, it is also noteworthy that the interfacial shear strength gets saturated with further increasing numbers of oxygenated groups, implying that the optimized functionalization degree is required to maximize the interfacial adhesion. Otherwise, the excess oxygenated groups grafted onto the graphene sheet might create defects in the graphene lattice and then compromise the mechanical properties of the individual graphene sheet itself.[48] Theoretical simulation based on molecular dynamics has observed about a 48% and an 183% increase of interfacial shear force in graphene with hydrogen and oxygen functionalization of 3%, respectively, compared to pristine monolayer graphene. Further increase of oxygen coverage up to about 7% led to a saturated interfacial shear force.[47] Herein, our experimental results are consistent well with the theoretical expectation, indicating that the optimization of functionalization degree is a critical issue to increase the interfacial shear strength without compromising intrinsic mechanical properties of graphene sheet in nanocomposites.

3.3. Failure Modes of the Oxidized Graphene/PMMA Nanocomposites at the Interface.

As mentioned earlier, for the vdW-dominated interface in the graphene/PMMA nanocomposite, the interfacial slippage initiates at edges at the critical strain level and then gradually propagates to the center of the graphene sheet with the increase of strain as shown in Figure 4a. Once the applied tensile strain is released, the interfacial shear stress would transfer in the opposite direction and apply compressive force to the graphene nanosheet. The formation of randomly distributed wrinkles and buckles as characterized by AFM in Figure S5h was due to the release of the compressive strain in the composite system. Particularly, in some cases, the bidirectional wrinkles rather unidirectional wrinkles were observed in Figure S5h, which could be attributed to Poisson's ratio effect during the loading/unloading, as well as the influence of geometry and orientation of individual graphene sheets with respect to the strain axis.[23] Comparatively, a monolayer graphene sheet with a moderate functionalization degree ($I_D/I_G = 3.5$) exhibited the similar interfacial failure modes as shown in Figure S4a, where both the compression-induced wrinkles and buckled delamination could be observed simultaneously as shown in Figure S4c. Owing to the enhancement of interfacial shear strength for the H-bonded interface system, the wrinkles in Figure S4c exhibited a larger height and wavelength compared with the vdW interface system (e.g., h = 9.1 nm, w = 169 nm vs h = 5.3 nm, w = 145 nm based on the averaged results of several locations). Moreover, the buckled delamination was also observed in both vdW interface and H-bonding interface systems as shown in Figure S5, panels h and i. The relatively large delamination height and width (h = 15.2 nm, w = 189 nm vs h = 5.3 nm, w = 145 nm) implies the improvement of the interfacial adhesion energy via the H-bonded interface.[29]

With further increasing the functionalization degrees of oxidized graphene sheets, the interfacial shear strength (τ_c) would reach a plateau as shown in Figure 5a. Meanwhile, the excessive oxygen-containing groups would create defects in the graphene lattice and weaken the mechanical properties of the individual graphene sheet.[48] To experimentally clarify such influence of an excessively functionalized graphene sheet on the interfacial properties as well as the failure mode of individual graphene sheet, herein, we monitor the strain distribution of the highly oxidized individual graphene sheet with $I_D/I_G = 5$ at various strain levels. Similar to the strain profiles of the oxidized monolayer graphene sheet with a moderate functionalization degree as shown in Figure S4a, at lower strain level, the interfacial shear stress can be efficiently transferred from matrix to the individual graphene sheet and the plateau strain of the oxidized graphene sheet carried is close to that of the matrix shown in Figure 6a. However, with further increasing strain level up to 0.7%, unlike the sliding behavior at the edges of the moderate functionalized graphene sheet as shown in Figure 4b and Figure S4a, a slight drop of the graphene strain at the plateau region occurred, indicating the initiation of the cracks. Once the strain up to 0.9%, the apparent drops of the graphene strain to low values are observed for the oxidized graphene sheet, indicating the permanent fracture of the oxidized monolayer graphene sheet. In comparison, no apparent drop of strain is observed for the graphene sheet with moderate functionalization degrees even suffered from high tensile strain levels. AFM was utilized to characterize the damage modes of the oxidized graphene sheet before the tension and after the release, respectively. As shown in Figure 6b, the oxidized monolayer graphene sheet initially presents the intactness with a relatively flat surface. Once subjected to axial tensile deformation up to 0.9%, several cracks perpendicular to the stretching direction are inclined to propagate in the oxidized graphene sheet shown in Figure 6c. The height profile across the cracks in Figure 6c pronouncedly displays the gaps at three marked sites, which was consistent with the obvious graphene strain dropped sites as shown in Figure 6a. Additionally, the Raman image of D-band intensity in Figure 6d after tensile deformation reveals that the cracks are prone to form at the sites with higher D-band intensity, implying that the excess oxygen-containing groups in the oxidized graphene sheet acted as defect sites to induce the initiation of cracks. In comparison, the buckled morphology was observed for the graphene sheet with moderate functionalization degree after mechanical unloading as shown in Figure S4c. The fracture mechanism of the oxidized graphene sheet could be further elucidated by the schematic drawing as shown in Figure 6e. The various oxygen-containing groups such as OH, C−O−C, or COOH grafted onto the graphene sheet during the oxidation process would naturally lead to configuration changes caused by orbital hybridization from a planar sp^2-hybridized geometry to a distorted sp^3-hybridized geometry.[49,50] Once the external load is applied to the highly oxygenated graphene sheet, the initiated or pre-existing defects are propagated perpendicular to the loading direction and resulted in catastrophic failure of the graphene sheet. With dependence on the functionalization degrees of the oxidized graphene sheet in this work, failure modes including the interfacial sliding, fracture of graphene sheet under tension, and buckling under mechanical unloading are identified and summarized in Figure S5. Such systematic investigation of the evolution of deformation modes of graphene fillers as a function of the functionalization degrees in nanocomposites has never before been reported.

4. CONCLUSION

In summary, the effect of the functionalization of nanofillers on the interfacial adhesion and the failure modes were examined first at the microscopic level for the monolayer graphene/PMMA nanocomposite system by means of in situ tensile micro-Raman and AFM technique. Due to the formation of H bonds between graphene and the PMMA matrix, the interface was strengthened with increasing functionalization degrees. The interfacial shear strength of the functionalized graphene was found to reach up to 1.7 MPa, which approximately quadrupled that of pristine graphene. However, distinct from the failure mode of interfacial sliding observed for the graphene sheet with moderate functionalization degree, excessive oxygen-containing groups would create defects in the graphene sheet and induce the crack initiation and propagation under tension. There is therefore a balance to be struck in the design of graphene-based nanocomposites between the ability to achieve higher interfacial adhesion and the reduction in the elastic modulus of the functionalized graphene sheet. The optimized functionalization degree is proposed to achieve the maximum effective modulus for the nanocomposite. The present work on the interfacial mechanics between graphene and PMMA could offer valuable insight and a design guideline for the enhanced functionalization of graphene with proper surface chemical groups as well as implementing reinforcing effects.

■ ASSOCIATED CONTENT

Supporting Information

The Supporting Information is available free of charge on the ACS Publications website at DOI: 10.1021/acsami.6b03069.

> Schematic diagram of PMMA cantilever beam, varied trend of Raman intensity ratio (I_D/I_G) as a function of the reaction times, interfacial parameters of tested graphene samples obtained from the nonlinear shear-lag model, stress-transfer behavior on the micro-mechanical level, monolayer graphene sheet with moderate functionalization degree (I_D/I_G = 3.5) as a reference, and summary of failure modes of graphene sheets with different functionalization degrees (PDF)

■ AUTHOR INFORMATION

Corresponding Authors

*E-mail: liulq@nanoctr.cn.
*E-mail: zhong.zhang@nanoctr.cn.

Notes

The authors declare no competing financial interest.

■ ACKNOWLEDGMENTS

This project was jointly supported by the National Key Basic Research Program of China (Grants 2012CB937503 and 2013CB934203) and the National Natural Science Foundation of China (Grants 51173030, 11225210, 21474023, 11222217, 11225421, 11434010 and 11474277).

■ REFERENCES

(1) Yu, M. F.; Files, B. S.; Arepalli, S.; Ruoff, R. S. Tensile Loading of Ropes of Single Wall Carbon Nanotubes and Their Mechanical Properties. *Phys. Rev. Lett.* **2000**, *84* (24), 5552−5555.

(2) Saito, R.; Dresselhaus, G.; Dresselhaus, M. S. *Physical Properties of Carbon Nanotubes*; World Scientific, 1998; Vol. 35.

(3) Lee, C.; Wei, X.; Kysar, J. W.; Hone, J. Measurement of the Elastic Properties and Intrinsic Strength of Monolayer Graphene. *Science* **2008**, *321* (5887), 385−388.

(4) Zhu, Y.; Murali, S.; Cai, W.; Li, X.; Suk, J. W.; Potts, J. R.; Ruoff, R. S. Graphene and Graphene Oxide: Synthesis, Properties, and Applications. *Adv. Mater.* **2010**, *22* (35), 3906−3924.

(5) Piggott, M. R. *Load Bearing Fibre Composites*; Springer Science & Business Media: 2002.

(6) Hull, D.; Clyne, T. *An Introduction to Composite Materials*; Cambridge University Press, 1996.

(7) Ramanathan, T.; Abdala, A. A.; Stankovich, S.; Dikin, D. A.; Herrera-Alonso, M.; Piner, R. D.; Adamson, D. H.; Schniepp, H. C.; Chen, X.; Ruoff, R. S.; Nguyen, S. T.; Aksay, I. A.; Prud'Homme, R. K.; Brinson, L. C. Functionalized Graphene Sheets for Polymer Nanocomposites. *Nat. Nanotechnol.* **2008**, *3* (6), 327−31.

(8) Hu, K. S.; Kulkarni, D. D.; Choi, I.; Tsukruk, V. V. Graphene-Polymer Nanocomposites for Structural and Functional Applications. *Prog. Polym. Sci.* **2014**, *39* (11), 1934−1972.

(9) Terrones, M.; Martin, O.; Gonzalez, M.; Pozuelo, J.; Serrano, B.; Cabanelas, J. C.; Vega-Diaz, S. M.; Baselga, J. Interphases in Graphene Polymer-Based Nanocomposites: Achievements and Challenges. *Adv. Mater.* **2011**, *23* (44), 5302−5310.

(10) Liu, L.; Barber, A. H.; Nuriel, S.; Wagner, H. D. Mechanical Properties of Functionalized Single-Walled Carbon-Nanotube/Poly (vinyl alcohol) Nanocomposites. *Adv. Funct. Mater.* **2005**, *15* (6), 975−980.

(11) Eitan, A.; Jiang, K.; Dukes, D.; Andrews, R.; Schadler, L. S. Surface Modification of Multiwalled Carbon Nanotubes: Toward the Tailoring of the Interface in Polymer Composites. *Chem. Mater.* **2003**, *15* (16), 3198−3201.

(12) Ajayan, P. M.; Schadler, L. S.; Giannaris, C.; Rubio, A. Single-walled Carbon Nanotube Polymer Composite: Strength and Weakness. *Adv. Mater.* **2000**, *12* (10), 750−753.

(13) Schadler, L. S.; Giannaris, S. C.; Ajayan, P. M. Load Transfer in Carbon Nanotube Epoxy Composites. *Appl. Phys. Lett.* **1998**, *73* (26), 3842−3844.

(14) Wagner, H. D.; Vaia, R. A. Nanocomposites: Issues at the Interface. *Mater. Today* **2004**, *7* (11), 38−42.

(15) Barber, A. H.; Cohen, S. R.; Wagner, H. D. Measurement of Carbon Nanotube−Polymer Interfacial Strength. *Appl. Phys. Lett.* **2003**, *82* (23), 4140−4142.

(16) Gao, Y.; Li, L.; Tan, P.; Liu, L.; Zhang, Z. Application of Raman Spectroscopy in Carbon Nanotube-Based Polymer Composites. *Chin. Sci. Bull.* **2010**, *55* (35), 3978−3988.

(17) Zhao, Q.; Wagner, H. D. Raman Spectroscopy of Carbon−Nanotube−Based Composites. *Philos. Trans. R. Soc., A* **2004**, *362* (1824), 2407−2424.

(18) Young, R. J.; Kinloch, I. A.; Gong, L.; Novoselov, K. S. The Mechanics of Graphene Nanocomposites: A Review. *Compos. Sci. Technol.* **2012**, *72* (12), 1459−1476.

(19) Ma, W.; Liu, L.; Yang, R.; Zhang, T.; Zhang, Z.; Song, L.; Ren, Y.; Shen, J.; Niu, Z.; Zhou, W.; Xie, S. Monitoring a Micromechanical Process in Macroscale Carbon Nanotube Films and Fibers. *Adv. Mater.* **2009**, *21* (5), 603−608.

(20) Ma, W.; Liu, L.; Zhang, Z.; Yang, R.; Liu, G.; Zhang, T.; An, X.; Yi, X.; Ren, Y.; Niu, Z.; Li, J.; Dong, H.; Zhou, W.; Ajayan, P. M.; Xie, S. High-strength Composite Fibers: Realizing True Potential of Carbon Nanotubes in Polymer Matrix Through Continuous Reticulate Architecture and Molecular Level Couplings. *Nano Lett.* **2009**, *9* (8), 2855−2861.

(21) Gao, Y.; Li, J. Z.; Liu, L. Q.; Ma, W. J.; Zhou, W. Y.; Xie, S. S.; Zhang, Z. Axial Compression of Hierarchically Structured Carbon Nanotube Fiber Embedded in Epoxy. *Adv. Funct. Mater.* **2010**, *20* (21), 3797−3803.

(22) Gao, Y.; Liu, L. Q.; Zu, S.-Z.; Peng, K.; Zhou, D.; Han, B.-H.; Zhang, Z. The Effect of Interlayer Adhesion on the Mechanical Behaviors of Macroscopic Graphene Oxide Papers. *ACS Nano* **2011**, *5* (3), 2134−2141.

(23) Frank, O.; Tsoukleri, G.; Parthenios, J.; Papagelis, K.; Riaz, I.; Jalil, R.; Novoselov, K. S.; Galiotis, C. Compression Behavior of Single-Layer Graphenes. *ACS Nano* **2010**, *4* (6), 3131−3138.

(24) Tsoukleri, G.; Parthenios, J.; Papagelis, K.; Jalil, R.; Ferrari, A. C.; Geim, A. K.; Novoselov, K. S.; Galiotis, C. Subjecting a Graphene Monolayer to Tension and Compression. *Small* **2009**, *5* (21), 2397−2402.

(25) Gong, L.; Kinloch, I. A.; Young, R. J.; Riaz, I.; Jalil, R.; Novoselov, K. S. Interfacial Stress Transfer in a Graphene Monolayer Nanocomposite. *Adv. Mater.* **2010**, *22* (24), 2694−2697.

(26) Young, R. J.; Gong, L.; Kinloch, I. A.; Riaz, I.; Jalil, R.; Novoselov, K. S. Strain Mapping in a Graphene Monolayer Nanocomposite. *ACS Nano* **2011**, *5* (4), 3079−3084.

(27) Gong, L.; Young, R. J.; Kinloch, I. A.; Riaz, I.; Jalil, R.; Novoselov, K. S. Optimizing the Reinforcement of Polymer-Based Nanocomposites by Graphene. *ACS Nano* **2012**, *6* (3), 2086−2095.

(28) Raju, A. P. A.; Lewis, A.; Derby, B.; Young, R. J.; Kinloch, I. A.; Zan, R.; Novoselov, K. S. Wide-Area Strain Sensors based upon Graphene-Polymer Composite Coatings Probed by Raman Spectroscopy. *Adv. Funct. Mater.* **2014**, *24* (19), 2865−2874.

(29) Jiang, T.; Huang, R.; Zhu, Y. Interfacial Sliding and Buckling of Monolayer Graphene on a Stretchable Substrate. *Adv. Funct. Mater.* **2014**, *24* (3), 396−402.

(30) Wang, G.; Liu, L.; Dai, Z.; Liu, Q.; Miao, H.; Zhang, Z. Biaxial Compressive Behavior of Embedded Monolayer Graphene inside Flexible Poly (methyl methacrylate) Matrix. *Carbon* **2015**, *86*, 69−77.

(31) Androulidakis, C.; Koukaras, E. N.; Frank, O.; Tsoukleri, G.; Sfyris, D.; Parthenios, J.; Pugno, N.; Papagelis, K.; Novoselov, K. S.; Galiotis, C. Failure Processes in Embedded Monolayer Graphene under Axial Compression. *Sci. Rep.* **2014**, *4*, 5271−5278.

(32) Geim, A. K.; Novoselov, K. S. The Rise of Graphene. *Nat. Mater.* **2007**, *6* (3), 183−191.

(33) Peng, K.; Liu, L. Q.; Li, H.; Meyer, H.; Zhang, Z. Room Temperature Functionalization of Carbon Nanotubes Using an Ozone/water Vapor Mixture. *Carbon* **2011**, *49* (1), 70−76.

(34) Timoshenko, S.; Gere, J. M. *Theory of Elastic Stability*, 2nd ed.; Dover Civil and Mechanical Engineering; Dover Publications, 2012.

(35) Dobb, M. G.; Johnson, D. J.; Park, C. R. Compressional Behavior of Carbon-Fibers. *J. Mater. Sci.* **1990**, *25* (2A), 829−834.

(36) Criegee, R. Mechanism of Ozonolysis. *Angew. Chem., Int. Ed. Engl.* **1975**, *14* (11), 745−752.

(37) Niyogi, S.; Bekyarova, E.; Itkis, M. E.; Zhang, H.; Shepperd, K.; Hicks, J.; Sprinkle, M.; Berger, C.; Lau, C. N.; deHeer, W. A.; Conrad, E. H.; Haddon, R. C. Spectroscopy of Covalently Functionalized Graphene. *Nano Lett.* **2010**, *10* (10), 4061−4066.

(38) Englert, J. M.; Vecera, P.; Knirsch, K. C.; Schäfer, R. A.; Hauke, F.; Hirsch, A. Scanning-Raman-Microscopy for the Statistical Analysis of Covalently Functionalized Graphene. *ACS Nano* **2013**, *7* (6), 5472−5482.

(39) Cancado, L. G.; Jorio, A.; Ferreira, E. H. M.; Stavale, F.; Achete, C. A.; Capaz, R. B.; Moutinho, M. V. O.; Lombardo, A.; Kulmala, T. S.; Ferrari, A. C. Quantifying Defects in Graphene via Raman Spectroscopy at Different Excitation Energies. *Nano Lett.* **2011**, *11* (8), 3190−3196.

(40) Zuo, S.; Wei, Y. Effective Elastic Modulus of Bone-like Hierarchical Materials. *Acta Mech. Solida Sin.* **2007**, *20* (3), 198−205.

(41) Zhang, R. F.; Ning, Z. Y.; Zhang, Y. Y.; Zheng, Q. S.; Chen, Q.; Xie, H. H.; Zhang, Q.; Qian, W. Z.; Wei, F. Superlubricity in Centimetres-Long Double-Walled Carbon Nanotubes under Ambient Conditions. *Nat. Nanotechnol.* **2013**, *8* (12), 912−916.

(42) Wang, W.; Dai, S.; Li, X.; Yang, J.; Srolovitz, D. J.; Zheng, Q. Measurement of the Cleavage Energy of Graphite. *Nat. Commun.* **2015**, *6*, 7853−7859.

(43) Zhu, H.; Zhu, S.; Jia, Z.; Parvinian, S.; Li, Y.; Vaaland, O.; Hu, L.; Li, T. Anomalous Scaling Law of Strength and Toughness of Cellulose Nanopaper. *Proc. Natl. Acad. Sci. U. S. A.* **2015**, *112* (29), 8971−8976.

(44) Gupta, A.; Chen, G.; Joshi, P.; Tadigadapa, S.; Eklund, P. Raman Scattering from High-Frequency Phonons in Supported N-Graphene Layer Films. *Nano Lett.* **2006**, *6* (12), 2667−2673.

(45) Putz, K. W.; Compton, O. C.; Palmeri, M. J.; Nguyen, S. T.; Brinson, L. C. High-Nanofiller-Content Graphene Oxide-Polymer Nanocomposites via Vacuum-Assisted Self-Assembly. *Adv. Funct. Mater.* **2010**, *20* (19), 3322−3329.

(46) Anagnostopoulos, G.; Androulidakis, C.; Koukaras, E. N.; Tsoukleri, G.; Polyzos, I.; Parthenios, J.; Papagelis, K.; Galiotis, C. Stress Transfer Mechanisms at the Submicron Level for Graphene/Polymer Systems. *ACS Appl. Mater. Interfaces* **2015**, *7* (7), 4216−4223.

(47) Zhang, Y. Y.; Wang, C. M.; Cheng, Y.; Xiang, Y. Mechanical Properties of Bilayer Graphene Sheets Coupled by sp(3) Bonding. *Carbon* **2011**, *49* (13), 4511−4517.

(48) Wang, M. C.; Lai, Z. B.; Galpaya, D.; Yan, C.; Hu, N.; Zhou, L. M. Atomistic Simulation of Surface Functionalization on the Interfacial Properties of Graphene-Polymer Nanocomposites. *J. Appl. Phys.* **2014**, *115* (12), 123520−123525.

(49) Schniepp, H. C.; Li, J. L.; McAllister, M. J.; Sai, H.; Herrera-Alonso, M.; Adamson, D. H.; Prud'homme, R. K.; Car, R.; Saville, D.

A.; Aksay, I. A. Functionalized Single Graphene Sheets Derived from Splitting Graphite Oxide. *J. Phys. Chem. B* **2006**, *110* (17), 8535−8539.

(50) Gómez-Navarro, C.; Burghard, M.; Kern, K. Elastic Properties of Chemically Derived Single Graphene Sheets. *Nano Lett.* **2008**, *8* (7), 2045−2049.